Geochemistry Geophysics Geosystems

G³

Tracking lava flow emplacement on the east rift zone of Kīlauea, Hawai'i, with synthetic aperture radar coherence

Hannah R. Dietterich

Department of Geological Sciences, University of Oregon, Eugene, Oregon 97403–1272, USA (hrd@uoregon.edu)

Michael P. Poland

Hawaiian Volcano Observatory, U.S. Geological Survey, Hawaii National Park, Hawaii 96718, USA

David A. Schmidt and Katharine V. Cashman

Department of Geological Sciences, University of Oregon, Eugene, Oregon 97403–1272, USA

David R. Sherrod

Cascades Volcano Observatory, U.S. Geological Survey, Vancouver, Washington 98683, USA

Arkin Tapia Espinosa

Department of Geosciences, University of Panama, Panama City, Panama

[1] Lava flow mapping is both an essential component of volcano monitoring and a valuable tool for investigating lava flow behavior. Although maps are traditionally created through field surveys, remote sensing allows an extraordinary view of active lava flows while avoiding the difficulties of mapping on location. Synthetic aperture radar (SAR) imagery, in particular, can detect changes in a flow field by comparing two images collected at different times with SAR coherence. New lava flows radically alter the scattering properties of the surface, making the radar signal decorrelated in SAR coherence images. We describe a new technique, SAR Coherence Mapping (SCM), to map lava flows automatically from coherence images independent of look angle or satellite path. We use this approach to map lava flow emplacement during the Pu'u 'Ō'ō-Kupaianaha eruption at Kīlauea, Hawai'i. The resulting flow maps correspond well with field mapping and better resolve the internal structure of surface flows, as well as the locations of active flow paths. However, the SCM technique is only moderately successful at mapping flows that enter vegetation, which is also often decorrelated between successive SAR images. Along with measurements of planform morphology, we are able to show that the length of time a flow stays decorrelated after initial emplacement is linearly related to the flow thickness. Finally, we use interferograms obtained after flow surfaces become correlated to show that persistent decorrelation is caused by post-emplacement flow subsidence.

1. Introduction

[2] Mapping of lava flows from the Pu'u 'Ō'ō-Kupaianaha eruption on the east rift zone of Kīlauea serves to document the ongoing eruption, while yielding insights into how lava flow fields develop [e.g., *Mattox et al.*, 1993; *Kauahikaua et al.*, 2003]. However, the locations, extents, and timing of flows are challenging to record with traditional field methods because of the large size and inaccessibility of the affected area. Remote sensing offers a means of gathering this information that circumvents these problems. Interferometric synthetic aperture radar (InSAR) is widely used to measure deformation by detecting minute changes in ground surface elevations at points that stay correlated during repeat observations [*Massonnet and Feigl*, 1998, and references therein]. Correlation of the radar echoes between two SAR acquisitions requires that the radar-reflecting surfaces within the radar footprint remain unchanged, permitting measurements of the line-of-sight change in range with InSAR. The eruption and emplacement of lava, however, changes the scattering properties of the surface, thereby disrupting the coherence of the radar echoes and precluding the application of interferometric techniques. Nevertheless, the abrupt change in surface properties where the ground is repaved by lava allows these new flows to be mapped with SAR coherence images [*Zebker et al.*, 1996]. We extend the application of coherence mapping to extract time-dependent flow maps from SAR coherence images. Our method, which we term SAR Coherence Mapping (SCM), is independent of look angle or satellite path, and it therefore allows synthesis of all available SAR data in a region to maximize the temporal sampling. We demonstrate the technique by examining the advance of lava flows in Hawai'i from 2003 to 2010, and explore ways that these data can be used to investigate lava flow behavior during and after emplacement.

[3] At many volcanoes around the world, lava flows are recurring natural hazards that impact populations and property. Mitigation strategies include both probabilistic approaches to hazard zone mapping [e.g., *Wadge et al.*, 1994; *Kauahikaua et al.*, 1995] and the development of models to address both conditions of lava flow advance [*Crisci et al.*, 1986; *Harris and Rowland*, 2001] and terrain analysis [*Kauahikaua et al.*, 2003]; the latter allow real-time decision-making in response to evolving eruptions. Observations of how flow fields develop over time are therefore crucial for tracking the path and velocity of flows, and for building an understanding of lava flow emplacement that is necessary for predicting future flow behavior.

[4] Flow mapping is the principal means of gathering information on the advance and morphology of active lava flows. Traditionally, active flows are mapped by ground-based field campaigns or airborne visual surveys [e.g., *Kauahikaua et al.*, 2003]. During the current east rift zone eruption of Kīlauea, the boundaries of new flows are recorded approximately weekly with handheld Global Positioning System (GPS) receivers for the whole flow, or more frequently as lava approaches populated areas (T. Orr, personal communication, 2012). Thermal imagery, in the form of forward-looking infrared (FLIR) collected from a helicopter or on the ground, or by a variety of satellites with infrared detectors, is also used to identify new flows. Repeat surveys constrain the aerial coverage and advance rates of active flows. These data are then used with flow thickness data to estimate volumes and average effusion rates.

[5] SCM can also be used to map lava flow emplacement and augments traditional mapping techniques in a few important ways. For example, direct access to the flows is not required and the state of the entire flow field is recorded in a single image. SAR also has the ability to see through cloud cover and is not limited to making observations during daylight hours. Additionally, the high spatial resolution and continuity of the satellite images yield more internal detail than GPS points collected along flow margins. Finally, a constellation of SAR satellites can collect images of the same region with greater frequency than the on-average weekly repeat time for field mapping. In real-time applications, ground-based methods are still critical given the lack of operational control in acquiring satellite images. Additionally, ground-based methods can better resolve flow fronts that enter vegetated regions and provide ground truthing of the coherence maps.

[6] The ability of SAR coherence to detect changes in the ground surface over time provides the basis for the lava flow mapping technique. SAR satellites

travel in repeating orbits and record radar echoes backscattered to the satellite from the surface. Surface change can be measured by comparing these radar echoes from two SAR scenes collected at different times from approximately the same viewpoint. Where the ground surface is identical between the two images, the radar echoes will have high coherence. However, where the surface has been altered between the acquisition dates of the images, it will have low coherence. This comparative property between SAR scenes can be defined mathematically as the correlation coefficient, a spatially averaged measurement of the similarity of the radar signals in phase and amplitude, with values between 0 and 1 [*Zebker and Villasenor*, 1992]. The correlation coefficients for each pixel combine to create a coherence image. Decorrelation is often associated with vegetation and water, whose surfaces change significantly between SAR acquisitions [*Zebker and Villasenor*, 1992]. Any variation in the viewpoint of the satellite between the SAR scene pairs also impacts the overall coherence of the images by changing the angle and arrangement of scatterers that the satellite sees. The perpendicular baseline, which is the distance between the satellite locations during the two SAR acquisitions, must therefore be limited for images to be sufficiently correlated [*Gatelli et al.*, 1994]. The length of time between SAR acquisitions further influences the overall coherence, because non-eruptive changes in the ground surface accumulate with time [*Lu and Freymueller*, 1998].

[7] New lava flows create decorrelation by repaving the ground surface over the extent of a flow, completely changing the ground's scattering properties between images collected before and after flow emplacement. However, once a flow becomes inactive, its surface remains stable between image acquisitions, yielding high radar coherence. Using these observations, *Zebker et al.* [1996] showed that coherence images of the active flow field on Kīlauea can be used to create flow maps, because decorrelated new flows are surrounded by highly correlated older flows. Therefore, new flow areas can be mapped by thresholding the image with a correlation value that represents the margin of the new flow [*Zebker et al.*, 1996]. This technique was also used to define flow boundaries from the 1995 Fernandina and 1998 Cerro Azul eruptions in the Galápagos [*Rowland et al.*, 2003], and the areal extent of the 1997 lava flow in the caldera of Okmok volcano [*Lu et al.*, 2000]. Similarly, non-lava sources of surface change, including pyroclastic flows at Soufrière Hills Volcano, Montserrat

[*Wadge et al.*, 2002], and the Portuguese Bend landslide in California [*Calabro et al.*, 2010], have been mapped with SAR coherence. In combination with InSAR, SAR coherence has also been used to measure post-emplacement behavior at lava flows on Okmok and Etna volcanoes. The 1997 Okmok lava flow and the 1986–1987, 1989, and 1991–1993 lava flows on Etna remained decorrelated for several years due to continued surface change from cooling, settling, and contraction [*Lu et al.*, 2000; *Stevens et al.*, 2001; *Lu et al.*, 2005]. Once a flow is correlated it is possible to extract a deformation signal with InSAR, which reveals post-emplacement subsidence [*Briole et al.*, 1997; *Stevens et al.*, 2001; *Lu et al.*, 2005].

[8] Our study builds on these previous mapping applications of SAR coherence by creating an algorithm to map successive lava flows from the ongoing Puʻu ʻŌʻō-Kupaianaha eruption of Kīlauea, Hawaiʻi. This eruption on the middle east rift zone of the volcano began in 1983 with episodic lava fountaining from the Puʻu ʻŌʻō vent that lasted until 1986. The eruption then continued through a constant effusion phase from the Kupaianaha vent from 1986 to 1992 and a nearly continuous effusion phase from Puʻu ʻŌʻō from 1992 to 2007, before shifting downrift to a vent between Puʻu ʻŌʻō and Kupaianaha called the "D" vent, because it was along Fissure D of the July 21, 2007 eruption, from 2007 to 2011 [*Heliker and Mattox*, 2003; *Poland et al.*, 2008; *Patrick et al.*, 2011; *Patrick and Orr*, 2012]. This eruption provides an ideal locality and event sequence to develop a SAR coherence flow mapping technique because of the multitude of flow field SAR scenes collected over time, the lack of snow or other environmental factors that could interfere with the radar detection of flows, and the detailed documentation of the eruption by the U.S. Geological Survey Hawaiian Volcano Observatory (HVO). By integrating a range of archived SAR data we assemble a detailed history of lava flow behavior at Kīlauea over an eight-year period, while developing an image analysis methodology to automate the detection of new flows. Our results provide flow emplacement data that suggest numerous potential applications of this technique to the study of lava flows around the world.

2. Methodology

2.1. SAR Data Sources and Processing

[9] We use 211 scenes from six tracks of Envisat SAR data (two ascending and four descending) to
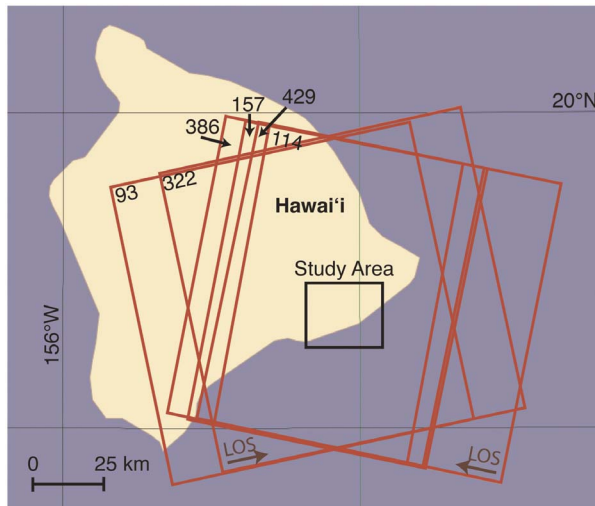
Figure 1. Location map of the study area on the east rift zone of Kīlauea, Hawai'i Island (Big Island), Hawai'i. Red boxes show the extents of Envisat SAR tracks and frames, while line-of-sight (LOS) vectors indicate the satellite look directions for ascending and descending tracks.

capture lava flow activity from January 2003 to October 2010 (Figure 1). Using the GAMMA processing package, we produce hundreds of coherence images between SAR scenes on respective orbital tracks for 35- to 105-day intervals (based on a 35-day repeat time), although the small number of SAR acquisitions early in the time sequence results in some coherence images with longer durations. To maintain overall coherence, we assemble coherence images only from SAR scene pairs with perpendicular baselines of less than 600 m. We maximize spatial resolution by processing the images at high resolution (one look in the range direction) and georectifying them with an oversampled digital elevation model (DEM) produced from the Shuttle Radar Topography Mission (SRTM) [*Farr and Kobrick*, 2000] to yield a final pixel size of 20 m. Finally, we crop the coherence images from all tracks to the same geographic extent, with each pixel assumed to represent an identical location on the volcano's surface.

[10] The coherence images document the degree of surface change (i.e., growth of vegetation, lava flows, etc.) over the duration of the image. Unlike deformation, which is directional and can only be measured along the satellite line of sight with interferometric SAR, the change in coherence from resurfacing is independent of the satellite viewpoint. This allows us to combine data from multiple tracks, and potentially even multiple SAR satellites,

and assemble a detailed time series with a much higher temporal resolution than a single track of any one satellite.

2.2. Image Analysis

[11] Our SCM technique combines and analyzes SAR coherence images to extract maps of lava flow activity with time, utilizing a series of image analysis algorithms in MATLAB®. The method maps new lava flows by thresholding the coherence images to identify decorrelated areas. Flow identification is complicated by nonvolcanic causes of decorrelation within the images, which must be masked out, and fluctuations in the overall coherence of the images, which require flexibility in the threshold value. Because coherence images from different tracks overlap in time, we can combine all of the images to create a time series, in which each time series frame spans one period of overlap, called a time series epoch. We then filter these time series frames to remove spurious results and thereby produce a final series of flow maps. The methodology is laid out in Figures 2 and 3, with the flowchart in Figure 2 displaying how an example initial coherence image from 2007 is processed and combined with overlapping images to create a time-dependent flow map.

2.2.1. Vegetation Removal

[12] The cropped original coherence images display the degree to which the surface has changed between two SAR scene acquisitions. Existing, stable flows have high radar coherence, or correlation values near 1, whereas active lava flows result in regions of very low coherence, with the mean correlation value of mapped flows equal to 0.13 ± 0.07 (1σ) (Figure 2a, step 1). However, coherence also tends to be low in vegetated areas and over water, requiring these features to be masked in the images. The coastline of the DEM used to process the coherence images masks the ocean. Vegetation could be masked with an independent map of vegetation at the start of the time series. Alternatively, we can create a vegetation map from the SAR data by assuming that these features stay decorrelated throughout the whole time series unless covered by lava. We determine the coherence levels of vegetated areas by calculating the average coherence over a 0.1 km^2 vegetated area in each image, and then use this to define a threshold to identify vegetated regions. We assemble an initial vegetation mask from pixels with values below this threshold in the first 26 coherence images (through November 2004). This captures persistently decorrelated areas
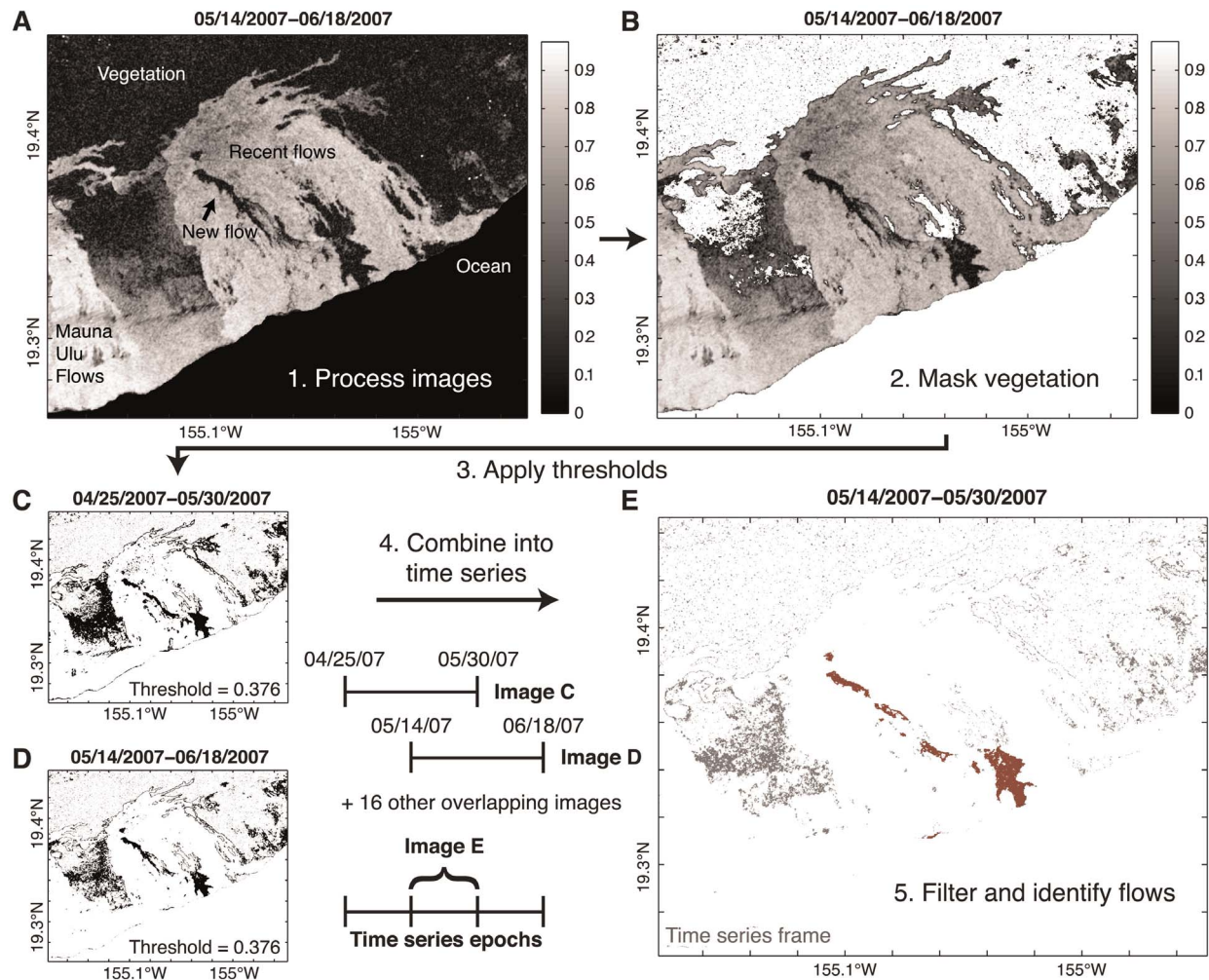
Figure 2. Flowchart of the SCM method. Image processing proceeds in the following order: (a) In step 1, a coherence image is produced from a pair of SAR scenes and displays the degree to which the scattering properties of the ground surface in each pixel have changed between May 14 and June 18, 2007. Areas that are unchanged have high coherence, with values near one, while regions with altered surfaces have low coherence, with values near zero. Correlated features including the 1983–2007 flow field, labeled "recent flows," and the Mauna Ulu flow field, can be identified in the image. Visibly decorrelated areas include vegetation beyond the edge of the flow fields, along with regions within the flow field that represent new activity. The ocean appears completely black in Figure 2a because it is masked by the extent of the DEM used to create the coherence image and represents a region of no data. (b) In step 2, vegetated areas within Figure 2a are removed with a vegetation mask to create an image where the remaining decorrelated pixels are potential lava flows. All pixels in the vegetation mask, as well as the ocean, have been made white. The vegetation mask for Figure 2a is built by creating an initial vegetation map, and then removing any pixels that are vegetated initially, but become correlated by the end date of the image (06/18/2007). (c and d) In step 3, multiple coherence images, each with its vegetation masked, are thresholded to select the most decorrelated pixels. The threshold applied to each image is a function of the perpendicular baseline, duration, and time of year of the images. For example, applying a threshold of 0.376 to Figure 2b produces Figure 2d, which is a binary image where pixels with values below the threshold are colored black. The offset timelines in the center show the temporal locations of the images in Figures 2c and 2d. In step 4, these two thresholded images (Figures 2c and 2d) combine with sixteen others that overlap the 05/14/07–05/30/07 time series epoch to produce (e) the time series frame (see Figure 3). Only pixels that are decorrelated in all eighteen images appear as gray or red in the time series frame. In step 5, by selecting only decorrelated areas of the time series frame that fall within the flow field and filtering out any regions that are within the scale of the noise (less than 0.008 km^2 in area) or represent sieve-like partially vegetated regions (area to perimeter ratios of less than 1.4, determined by trial and error), we isolate the final flow map for the 5/14/07–5/30/07 epoch, shown in red in Figure 2e.
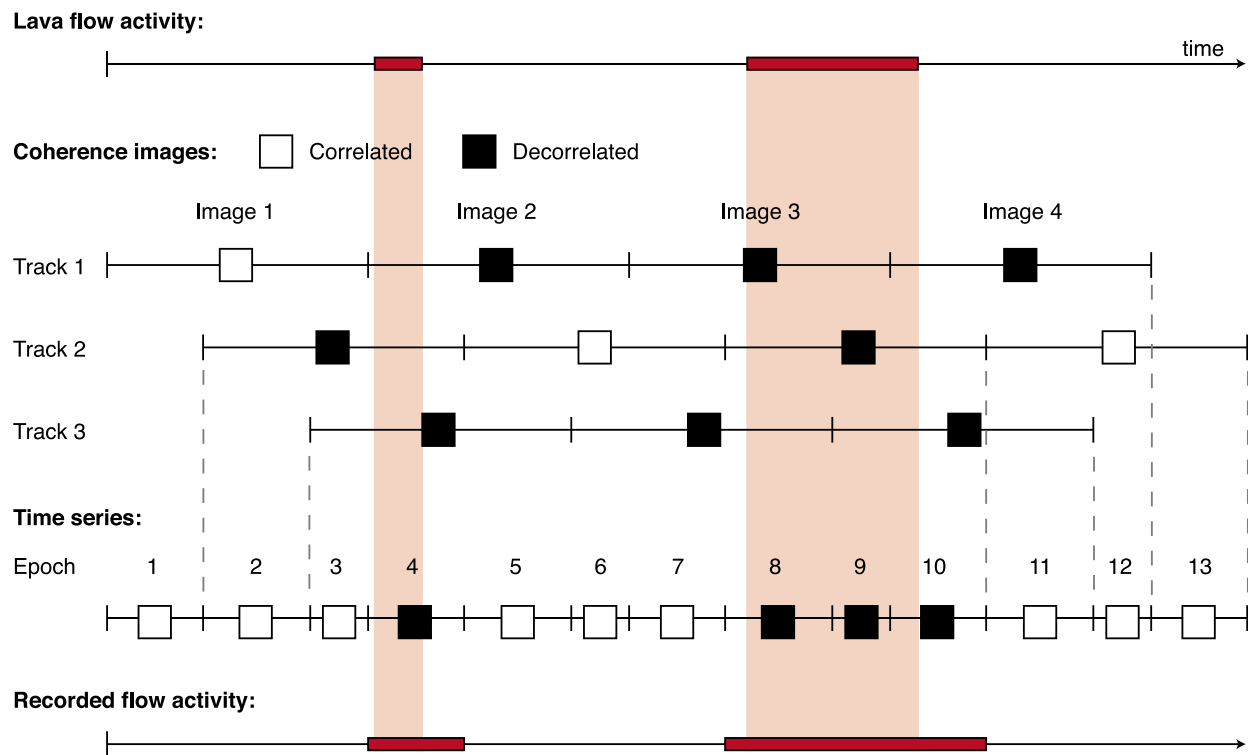
Figure 3. Schematic demonstration of how the time series inversion captures flow activity over a single pixel. Two hypothetical lava flows over the pixel are shown in the first timeline. These cause decorrelation in the coherence images (shown as timeline segments) that span their emplacement in three simulated satellite tracks. The tracks each record the same activity, but are offset in time, allowing us to combine them to produce a time series with greater temporal resolution, divided into epochs. Each epoch spans the time between each SAR scene, regardless of its track. The pixel is defined as decorrelated during the epoch only if it is decorrelated in all images that overlap the epoch in time. In this way we are able to document the flow activity with great accuracy and better resolution than a single satellite track.

that represent the extent of the vegetation at the beginning of the time sequence.

[13] As flows penetrate the vegetation at the margins of the flow field, the vegetation mask must shrink accordingly. Once a flow enters vegetation and becomes inactive, the flow becomes correlated. Therefore, if pixels that are part of the vegetation mask become correlated, a lava flow must have been emplaced in the previous time step. The algorithm accounts for this by assembling a dynamic vegetation mask that is modified through time, removing pixels from the mask for a given image that are correlated in any of the coherence images that overlap or immediately follow it in time (Figure 2b, step 2). This allows pixels that become correlated in the next time step to be identified as lava flows in the current time step.

2.2.2. Image Thresholding

[14] With the vegetation and ocean masked, the decorrelated areas within the images should represent lava flows. These flows are identified by applying

a threshold to the newly masked images to create a binary image, with the pixels of interest below a threshold correlation assigned values of 1, and all others assigned a value of 0 (Figure 2, step 3). However, because each of the coherence images was created from a slightly different orbital geometry and surface condition, the threshold correlation value that marks the margin of a flow varies from image to image. We therefore calculate a unique threshold for each masked correlation image based on the perpendicular baseline, duration, and time of year of the image.

[15] We compute the threshold by measuring the average value of four 0.1 km² areas of existing flows at widespread locations within the image and fitting curves to these average correlation values plotted against baseline, duration, and the start date of the image. We find that none of these variables exerts a strong influence on the coherence of the images, in contrast to locations such as Alaska that have a strong seasonal signal [Lu and Freymueller, 1998]. The effects of elevation, rainfall, and slope

were also tested but revealed little influence. Only the pali, a steeply sloping terrain where lava flows have covered a large fault scarp, has poor coherence, and only at long baselines.

[16] Through this process, each image is assigned a unique threshold value based on the set of calibration variables, with an average threshold value of 0.36 for the entire suite of images. For each masked coherence image, the corresponding binary images highlight the decorrelated features that do not fall within the vegetation mask (Figures 2c and 2d).

2.2.3. Time Series Assembly

[17] The thresholded images identify resurfacing of the ground surface within 35 to 350-day windows between SAR acquisitions on each track. Although the thresholded images can only be produced from SAR scene pairs within the same track, the tracks are offset in time, making it possible to create a new time series of images that represents the areas that are decorrelated where images from any track overlap in time (Figure 2e, step 4). Figure 3 demonstrates schematically how this time series inversion produces an image between each consecutive pair of SAR acquisition dates, which we call time series epochs. The combination of the tracks into a time series is based on the principle that every thresholded image that spans the period of the emplacement of a lava flow must be decorrelated over the extent of the flow. Therefore, only pixels that are decorrelated in all of the thresholded images that overlap with a given time series epoch are mapped as decorrelated within the epoch. Because this removes pixels that are not consistently decorrelated over a time series epoch, it acts to filter out noise from areas with correlation values barely below the threshold. Importantly, it allows us to record lava flow activity at higher temporal resolution than a single track would permit. However, lava flows that have entered (decorrelated) vegetation are identified only when they become correlated. For this reason, the extent to which flows have advanced into vegetation can be mapped only retroactively, and may therefore overlap in time with images that are fully correlated. To account for this difference, pixels that become correlated between the start and end of each time epoch (i.e., those pixels that represent flows that entered vegetation) are added to the time series image for that epoch to create the final flow map.

2.2.4. Flow Identification

[18] Despite these image processing techniques, each time series frame shows some level of scatter in the signal that does not correspond to the active flows during the epoch (shown as gray pixels in Figure 2e). One significant source of error is decorrelation in some time series frames due to the steep slopes of the pali. By using the DEM to mask out parts of the image where the slope is greater than 18°, the worst of this noise is eliminated. We then assume that during an epoch, new lava will occupy a contiguous region within the flow field, as defined by a simplified polygon. A filter based on the areas and perimeters of these regions removes local noise and the sieve-like areas of partial vegetation that are occasionally decorrelated. These filters allow us to map regions that fit the previously defined criteria, have an area greater than 0.008 km^2 (20 pixels), and an area to perimeter ratio of greater than 1.4, as lava flows. Perimeters calculated in this analysis represent the distances between the centers of adjoining edge pixels, while areas include the full pixel extent. Threshold values for area and the ratio of area to perimeter were determined from trial and error to remove known noise without eliminating known lava flows. This image analysis algorithm produces a flow map such as that shown in red in Figure 2e.

3. Results

[19] Each of the 210 flow maps displays the activity associated with Kīlauea's east rift zone eruption over an epoch; epochs range in duration from 1 to 137 days, with an average of 13.4 days. When viewed chronologically, the maps show the progression of the eruption from January 2003 to October 2010 (Animation S1 in the auxiliary material).[1] The maps can be grouped by the major episodes as documented by HVO (Figure 4). Here flows are colored according to time sequence, with blue being the oldest, and red the youngest, of each time period. We then compare our composite flow maps with composite flow maps from HVO (Figure 5).

[20] The flows active over the first year and a half of the time sequence, from January 20, 2003 to July 21, 2004 (Figure 4a), belong to episode 55 of the Pu'u 'Ō'ō-Kupaianaha eruption, which began in 1997 and lasted until 2007. During this part of episode 55, flows traveled down the western margin of the flow field (blue flows) and then found a different path to the ocean in 2004 (red flow). Rootless shields [*Kauahikaua et al.*, 2003] over the lava tube were active during the entire period and
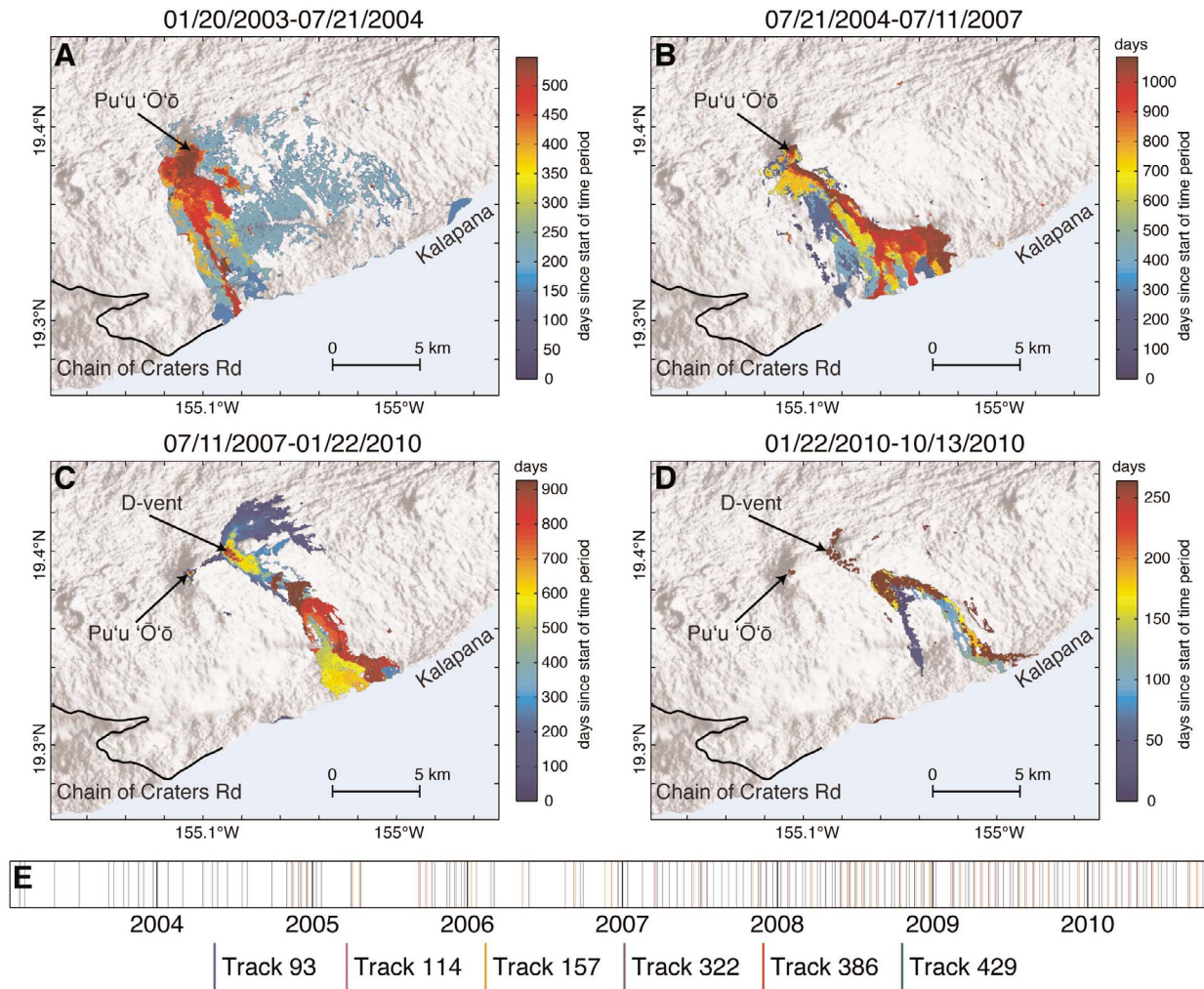
Figure 4. All 210 flow maps in the time series are displayed in four panels over the SRTM DEM [*Farr and Kobrick*, 2000]. Within each, the oldest maps are shown in dark blue grading up to the newest maps in maroon, with the number of days since the start of the panel shown on the adjoining color scale. (a) Middle part of episode 55. The large decorrelated regions in light blue are due to noise. The hourglass shape to the east of the main flows reveals persistent activity at several rootless shields that became quiet in August 2002. (b) The latter part of episode 55. Continued activity and persistent decorrelation of the flows emplaced during the interval shown in Figure 4a can be seen in the dark blue areas to the west of the main flows. (c) The July 21, 2007 flow and the Thanksgiving Eve Breakout (TEB) of episode 58. The July 21, 2007 D-vent in the southwest part of the July 2007 flow field and breakouts along the tube are apparent. (d) Continued breakouts from the TEB tube produce the March to October 2010 flows along the eastern margin of the TEB flow field. The extensive decorrelation in the final maroon map is noise. (e) A timeline of the study period displays the temporal distribution of SAR scenes. Note the lower density of scenes toward the beginning of the time sequence.

are delineated by the zone of decorrelation to the south and east of Puʻu ʻŌʻō. Older rootless shields formed in 2002 appear as an hourglass-shaped region of decorrelated pixels southeast of Puʻu ʻŌʻō. The widespread blue regions of decorrelation (Figure 4a) are due to noise and not included in the following analysis. Immediately to the southeast of Puʻu ʻŌʻō, the red flows represent the earliest stage of the next period of activity.

[21] The period from July 21, 2004 to June 17, 2007, corresponding to the last three years of episode 55, was marked by activity within a flow field and set of tube systems distinct from those of previous flows (Figure 4b). Lava flows generally migrated from west to east during this period and created many different ocean entries. West of these 2004–2007 flows, the narrow 2004 flow is still evident as a chain of blue pixels in the flow maps.
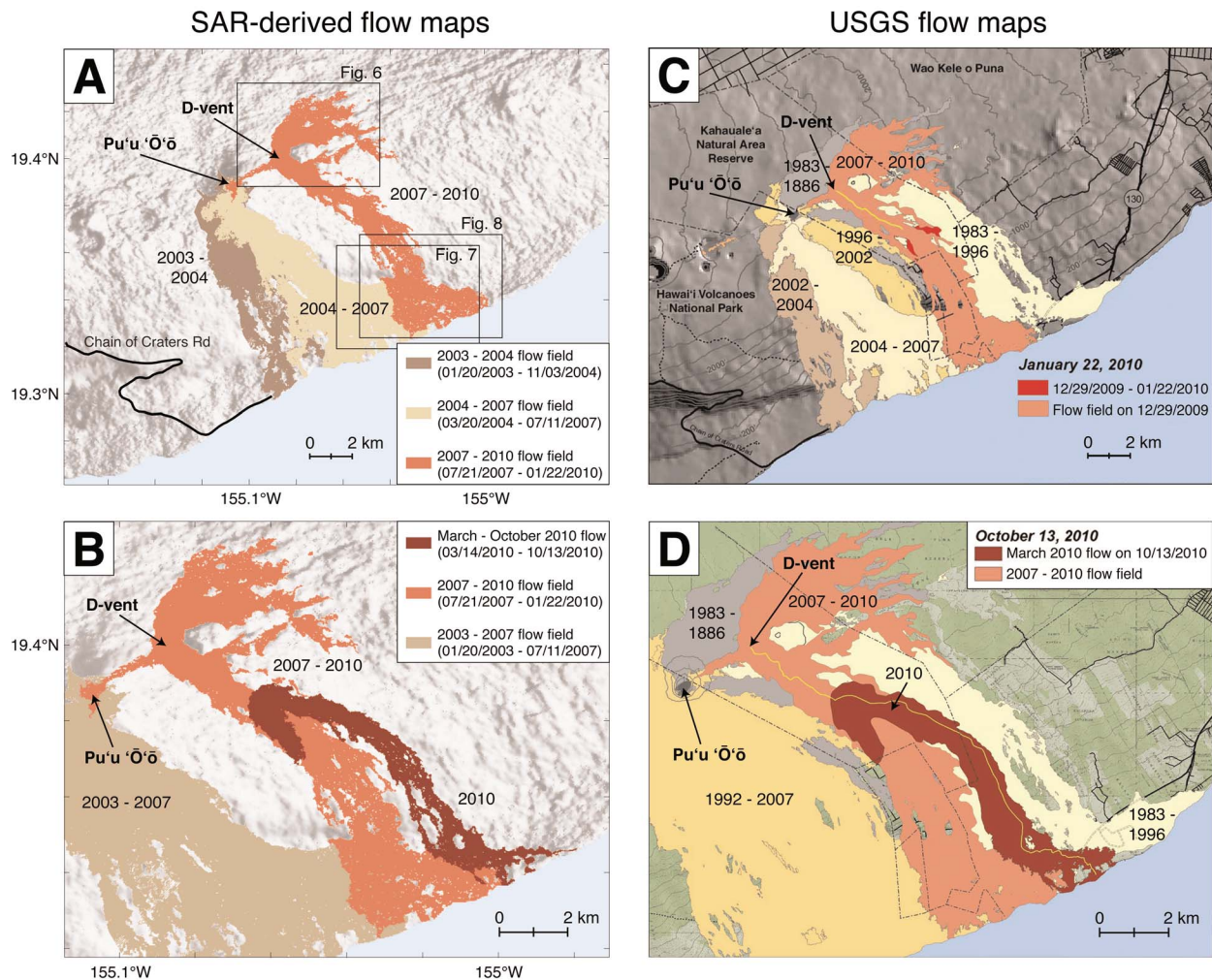
Figure 5. (a) SCM flow map summarizing flow field activity from January 2003 to January 2010. The colors show the different eruption episodes as defined by the USGS. The extents of Figures 6–8 are shown as black outlines. (b) SCM flow map of flow field activity from July 2003 to October 2010, displaying combined pre-2007 flows, the July 2007 to January 2010 flow field, and the March to October 2010 flow. (c) USGS flow map of activity from 1983 to January 2010, corresponding with Figure 5a. (d) USGS flow map highlighting the 2007 to 2010 flow field and the March to October 2010 flow, for comparison with Figure 5b.

The rootless shields above the tube from the previous period are also decorrelated and remain so until late 2006. During July 17–19, 2007, an intrusion and small eruption occurred uprift of Puʻu ʻŌʻō—Episode 56 of the long-term east rift zone activity. After an 11-day pause, lava reappeared at Puʻu ʻŌʻō on July 1 and began refilling the cone (Episode 57) [*Poland et al.*, 2008]. Neither of these episodes are specifically identifiable in the flow maps.

[22] On July 21, 2007, activity shifted from Puʻu ʻŌʻō to a series of fissures in the northeast part of the flow field to mark the start of episode 58 of the Puʻu ʻŌʻō-Kupaianaha eruption [*Kauahikaua*, 2007]. Within a few days the eruption localized at a single

vent—the July 21, 2007 D vent—and began feeding lava to the northeast, eventually forming a 2-km-long perched lava channel [*Patrick et al.*, 2011]. Northeast-directed flows lasted until November 21, 2007, as shown by the dark blue flows in Figure 4c. At this time, the flow direction changed when a breakout at the D-vent initiated the Thanksgiving Eve Breakout (TEB) flow, which formed a new lava tube to the ocean [*Patrick and Orr*, 2012]. Breakouts from this tube occurred throughout 2008–2010. The source of the TEB flow, and the rootless shield complex that formed along the lava tube to the southeast, remained decorrelated through 2009. Breakouts along the tube yield a chain of fan-shaped regions of decorrelation, but the tube itself is correlated, and therefore not

mapped with SCM. The advance of some of the breakouts to the ocean can be seen in the progressive color change along the individual flows.

[23] The last nine months of the time sequence are dominated by breakouts from the TEB lava tube between January 22 and October 13, 2010 (Figure 4d). Early in this period, a breakout that initiated in January traveled south from the vent but failed to make it to the coast (shown in blue). On March 12, a larger breakout started feeding a flow to the southeast. Once established, the tube system of the March 2010 breakout transported lava to the ocean on several separate occasions between April 2010 and until the end of the time series. This flow is highlighted in Figure 5b for comparison with the flow map produced by HVO.

4. Discussion

4.1. Evaluation of Results

[24] To assess the accuracy of the maps produced by SCM we compare them to the maps created by HVO. The coherence maps (Figures 5a and 5b) correspond well to the USGS maps produced using both aerial and field surveys (Figures 5c and 5d). In detail, however, there are some differences between the SAR-generated and field-generated flow maps. First, in Figures 5a and 5c, the northwestern-most lobe of the 2004–2007 flows is not fully captured by the SAR because these flows were emplaced on top of the rootless shields from the 2002–2004 flows, which had not yet become correlated. Second, a comparison of Figures 5b and 5d shows differences in the detail and extent of the March–October 2010 flow over the pali. This is caused by the difference in spatial resolution between the SAR and the USGS data. Satellite imagery is spatially continuous, whereas field mapping is often limited to the flow margins. The internal structure of the active flows, including the kīpuka, is therefore imaged more completely in the SCM maps. We examine this point in more detail below. It is also important to note that Figures 5a and 5c are not directly comparable because of the absence in the SCM map of flows emplaced before 2003, when the coherence time series begins.

4.1.1. Errors in SAR-Based Mapping

[25] Early in the time series, there are many fewer SAR acquisitions, reducing the number of overlapping images and the temporal resolution (Figure 4e). This led to problems with some of the early flow maps, which are quite noisy and therefore were not included in the summary maps (blue regions in Figure 4a). Limited image acquisition meant that each map was produced using only one coherence image. The SCM technique works best when many images overlap a time epoch and can therefore be combined to filter out noise from images with poor coherence or decorrelated regions due to steep topography.

[26] Another source of error relates to difficulties in generating SAR-based flow maps in vegetated regions, as illustrated by the mismatch of maps showing the northeastern July 2007 flow (Figures 5a and 5c). This highlights a major weakness of SCM. Although vegetated pixels can be mapped as lava once they become correlated, many of these pixels do not appear in the final maps, because the flow does not become correlated all at once; instead, parts of the flow remain decorrelated for longer periods than others. When this happens, our flow identification algorithm filters out parts of these flows that are small in size and spatially isolated.

[27] Our ability to map flows into vegetation therefore depends on how long the flow stays decorrelated. Flows that travel into vegetation can only be mapped after they become correlated, which may be months after emplacement. This prevents mapping flows into vegetation in near-real time. We illustrate this problem by comparing an SCM flow map from July to October 17, 2007 with a flow map from a field survey that we conducted on October 16, 2007 (Figure 6a). This comparison shows that the coherence-derived flow map is confined primarily to the previously non-vegetated areas, the exception being flow lobes within the vegetation that had become correlated by October. Flow lobes that remained decorrelated for long time periods (up to 2.5 years) are not fully mapped because of the piecewise manner in which the flow becomes inactive and correlated.

[28] Possible solutions to this vegetation problem include independent measurements of flow extent from thermal imagery or other mapping to document the true flow margins. Alternatively, the addition of SAR imagery from another satellite with a longer wavelength has enormous potential to both solve the vegetation problem and enhance the temporal detail of the time series. We demonstrate this potential with an image from the ALOS satellite, which uses a wavelength of 23.6 cm (L-band), compared to the 5.6 cm wavelength of the C-band Envisat satellite. The longer wavelength makes it less sensitive to minor changes in the ground surface and increases the
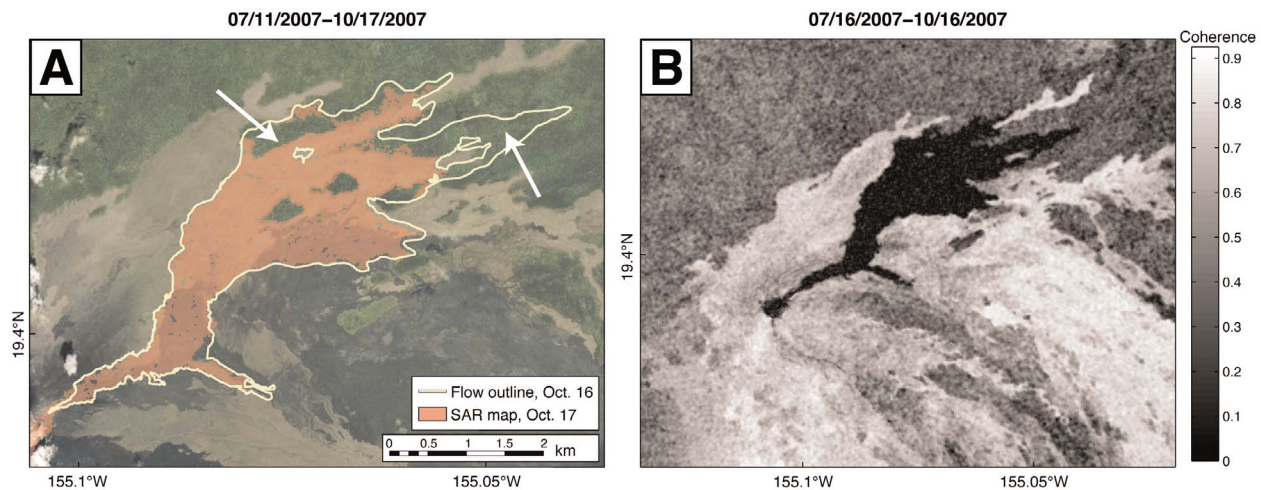
Figure 6. (a) The SCM map of the July 2007 flow extent as of October 17, 2007 (pink) is overlain on a pre-eruptive satellite image, and compared to the flow extent mapped on October 16 (yellow outline). The SCM technique cannot detect the flow where it enters vegetation, except where it has become inactive and correlated (older kīpuka in the center and white arrows). Even once the entire July 2007 flow becomes correlated, SCM fails to capture the full extent (compare to Figure 11 SCM map extent). (b) ALOS coherence image of the July 2007 flow field from July 16 to October 16, 2007. The longer wavelength (L-band; 23.6 cm) of the ALOS satellite yields higher coherence of the vegetation, allowing the discernment of the full extent of the July 2007 flow into the vegetated regions. Incorporation of ALOS data into this technique has the potential to solve the problem of mapping flows into vegetation.

coherence of vegetated areas [*Zebker et al.*, 1997]. For this reason, the decorrelation signal of the active lava flows is more easily recognized (Figure 6b). The longer wavelength, and therefore lower sensitivity, also yield a quicker return of the flow to correlation.

4.1.2. New Views From SAR-Based Mapping

[29] The SCM technique contributes new insight into flow emplacement processes in that it goes beyond mapping the surface flow margins that have been meticulously documented by the USGS. This is because decorrelated pixels not only indicate new surface flows, but also lava tubes, ocean entries, and eruptive vents, which are areas of strong deformation and numerous small breakouts. An example of internal detail within the margin of a flow being captured by SCM is demonstrated by a comparison of a SAR-based flow map to USGS tube and flow margin maps from May to June 2007 (Figure 7). The SAR-based flow map shows extensive activity near the ocean entry over its 19-day duration. The origin of this decorrelation can be determined by examining a short-wavelength infrared (SWIR) image from the ALI instrument on the EO-1 satellite that captures thermal activity on the flow field at an instant in time. Here hot spots in the SWIR image (yellow dots in Figure 7) lie directly on top of the edges of the SAR-mapped

flows near the coast, in addition to areas on the tube. This correspondence confirms that much of the extensive area of decorrelation near the ocean entry is caused by numerous breakouts.

[30] Lava tubes, which can be difficult to map in the field without the aid of thermal imaging, can also be observed in some of the coherence images. Once a tube is established below a roof of inactive flows, it becomes sufficiently correlated to be omitted from the final flow maps. However, active lava tubes can often be identified as a moderately decorrelated path through the flow field in the original coherence images (Figure 8). The reduced coherence of the tube is likely a product of deformation and disturbances of the surface over the tube, which may occur during inflation of filled tubes or by changes in flux through open tubes [e.g., *Kauahikaua et al.*, 1998, 2003; *Orr*, 2011].

[31] Finally, coherence maps highlight breakouts and active regions contained within an active flow field, which are details that are not generally included in USGS maps. For example, the SAR- and field-based maps of the March to October 2010 flow (Figures 5b and 5d) are similar in outline but quite different in internal flow structure. To evaluate the source of this difference, we compare a single (3-day) coherence flow map with an (instantaneous) oblique FLIR image from early May 2010 (Figure 9)
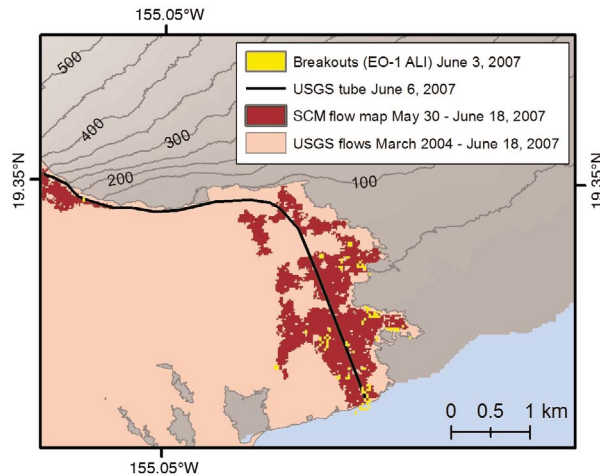
Figure 7. The SCM flow map from May 30 to June 18, 2007 (red) lies within the boundary of the USGS map from June 13, 2007 (pink) (T. Orr, personal communication, 2012). The SAR displays activity over the lava tube (black) and the ocean entry, where severe deformation and breakouts can cause decorrelation. Yellow regions display the hottest pixels from a short-wavelength infrared satellite image collected by EO-1 ALI on June 3, 2007. These hot areas represent active breakouts and correspond well to locations of SAR decorrelation.

(M. Patrick, personal communication, 2012). This comparison shows that each individual decorrelation region of the March to October 2010 flow corresponds to an active or recently active breakout, as shown by hotter surface temperatures (warmer colors) of the FLIR image. Other regions of the flow are both cooler and correlated, despite an active lava tube beneath the surface. The flow map does not extend all the way to the 2010 coastline, which has been built by new lava deltas since 2000, when the DEM used to create the coherence images was created.

[32] In summary, we find that SAR-based flow maps correspond well with field-based maps except where flows enter vegetated regions (or form new lava deltas, e.g., Figure 9). Problems in mapping lava entry into vegetated regions can be alleviated by using longer wavelength (L-band) SAR images. We also show that SAR-based flow maps provide detailed views of flow emplacement, because they highlight active regions inboard of flow margins that are often inaccessible from the ground. These include active lava tubes and surface breakouts. SCM thus complements both traditional flow mapping techniques and more recent thermal imaging strategies, which are limited by cloud cover (satellite-based thermal imaging) and spatial extent (handheld or helicopter-mounted FLIR cameras).

4.2. Analysis and Applications

[33] The ability to map lava flows at high spatial and temporal resolution has numerous potential applications to the study and monitoring of volcanoes. We have demonstrated that flow maps generated by SCM offer insights into planform flow morphology, which is useful for characterizing flow emplacement behavior. Flow lengths, widths, and areas can be measured as on any map and time sequences provide information on flow advance rates. For example, the TEB event produced a flow that reached the ocean on March 5, 2008. Its progress can be documented with the SCM maps from the time of its breakout (constrained by SCM between November 21 and November 25, 2007) until it reached the ocean (constrained by SCM between March 5 and March 13, 2008). Initial average rates of flow advance were 2.4 m/hr; flow advance then accelerated to 13.6 m/hr (Figure 10). These data agree with estimates from field mapping (Figure 10, inset) (M. Patrick, personal communication, 2012), except in the length of the western branch of the flow. Near its final extent, this branch traveled through vegetation and narrowed, preventing SCM from identifying its full length. Flow advance rates can be calculated with SCM only for flows that are emplaced over more than one time epoch; thus, they are time-averaged rates applicable
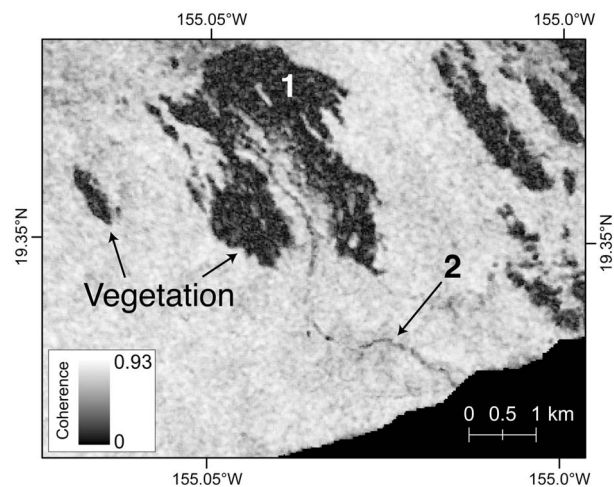

Figure 8. View of the pali and coastal plain in a coherence image from 07/28/2009 to 10/06/2009. The fully decorrelated area in the center (indicated by 1) shows breakouts over the pali near the Royal Gardens subdivision. The thin line of moderately decorrelated pixels leading from these breakouts to the coast (indicated by 2) reveals the path of a lava tube. The route matches well with USGS mapping of the tube from the summer of 2009 (T. Orr, personal communication, 2012).
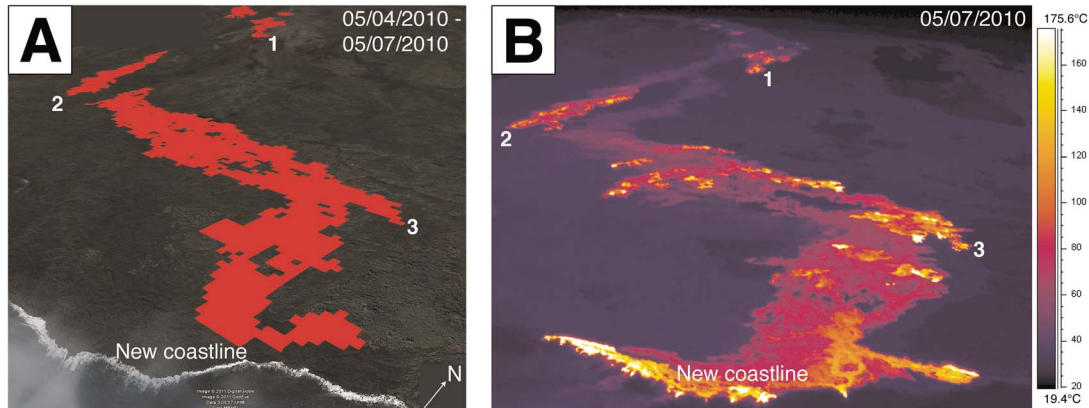
Figure 9. (a) Oblique view of the SCM flow map (looking toward the northwest) from May 4 to May 7, 2010 draped over topography and a satellite image. (b) FLIR image collected on May 7, 2010 from a helicopter looking upslope to the northwest (M. Patrick, personal communication, 2012). The colors show approximate surface temperature, with the hottest colors representing new breakouts of lava. Locations 1, 2, and 3 mark common features in the images. Decorrelated pixels (red) correspond to new and recent breakouts, while cooler, existing parts of the flow appear correlated. The different coastlines of the SCM map and 2010 imagery show the growth of the island into the ocean, because the SCM map is limited to the extent of the 2000 coastline.

to flows with durations of days or months, rather than hours. The final length of the TEB flow as of July 7, 2008 is 12 km, with an average width of 550 m, and a total area, including the July 2007 flow extent, of 16 km². This total area is less than the 21 km² mapped in the field (T. Orr, personal communication, 2012) because the SCM technique missed regions where the flows went into vegetation.

[34] SCM lava flow maps also provide important information on other aspects of lava flow emplacement. Particularly intriguing is the wide variation in the time over which different parts of a flow remain decorrelated after initial emplacement. This variation is particularly apparent in the northeastern flows that were emplaced in 2007 [Patrick et al., 2011], where decorrelation durations range from 13 to 903 days. When examined in map view, it is clear that the center of the flow remained decorrelated much longer than the edges (Figure 11).

[35] To test the extent to which this decorrelation pattern reflects variations in flow thickness, we overlay our flow thickness data onto the SAR decorrelation map (Figure 11). The thickness data were acquired in mid-October 2007 by kinematic GPS using Leica SR520 receivers carried on numerous traverses while sampling at 1 Hz frequency. Base station data came from nearby continuous GPS stations. The kinematic data (x, y, z) are accurate to within a few centimeters. Each traverse started and ended a few meters off the new lava flows so that altitudes could be correlated with SAR digital elevation data acquired in 2005.

[36] Flow thickness correlates reasonably well with decorrelation time (Figures 11 and 12), with the thickest area of the flow showing an average decorrelation duration of 375 days, compared to
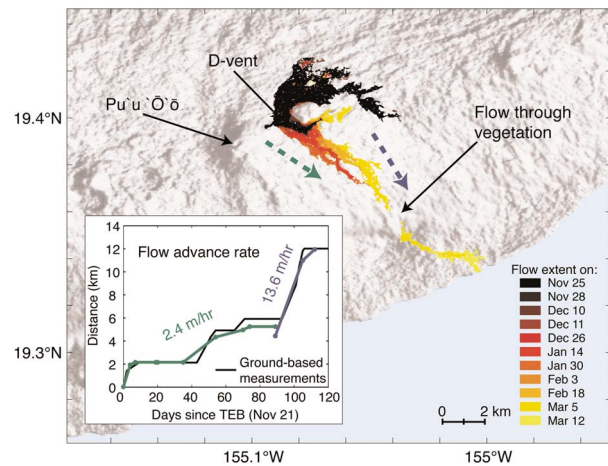

Figure 10. The extent of the Thanksgiving Eve Breakout flow, which began November 21, 2007, is displayed with time. From this map we can calculate the advance rate of the flow, shown in the inset plot of the length of the flow with time. Our data mostly compare well with field-based advance data plotted as a black line (M. Patrick, personal communication, 2012), with the exception of the distal extent of the western branch, plotted in green. The end of this flow is lost with SCM due to its passage through vegetation and narrow morphology. The flow accelerates as it advances over the pali.
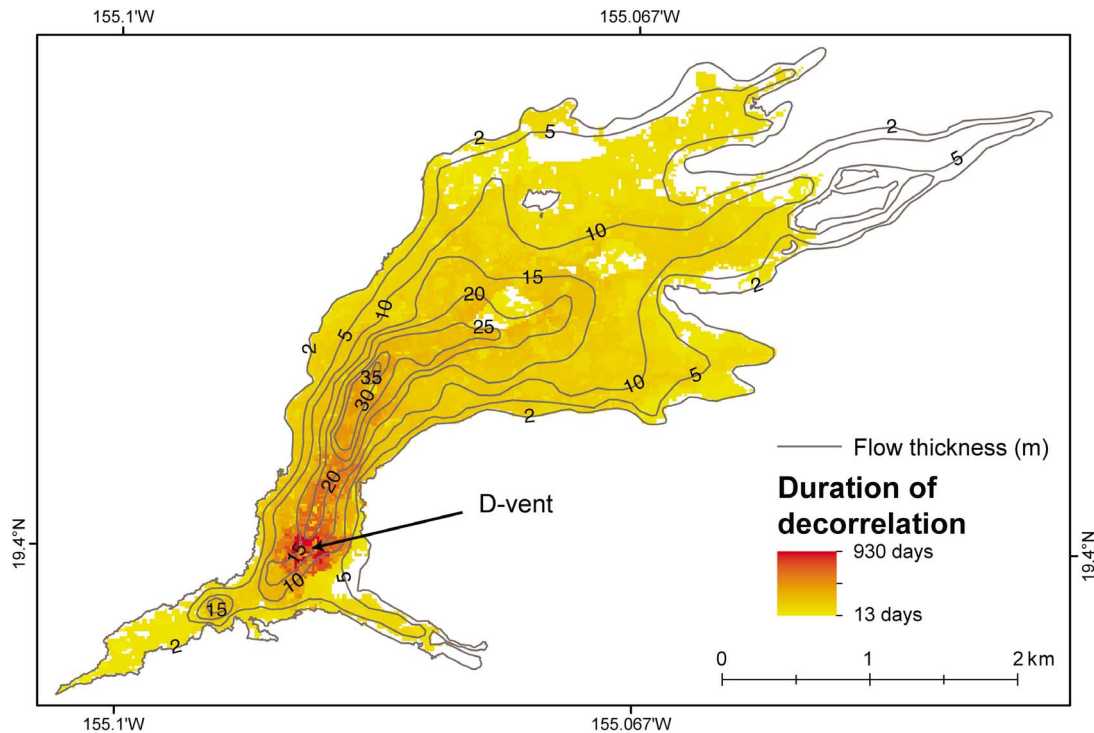
Figure 11. The length of time each pixel in the July 2007 flow is decorrelated after initial emplacement matches well with the surveyed flow thickness contours from October 16, 2007. The thickest part of the flow, 35 m, is decorrelated an average of 375 days and corresponds to the perched lava channel [*Patrick et al.*, 2011], whereas the thinnest, 2-m-thick flow margins are decorrelated for an average of 94 days. The area of the flow just south of the thickest section is decorrelated the longest, up to 903 days, because it is the source of the TEB flow in November 2007 (July 21, 2007 D-vent), where activity persisted long after the rest of the July–November 2007 flow field became correlated. Where the flow entered vegetation and was recovered by the flow-mapping algorithm, the decorrelation duration is a minimum, because it only represents the duration of the epoch prior to when the flow became correlated. This yields the yellow holes within the orange region in the center of the flow.

94 days within the thinnest regions. The thickest part of the flow corresponds to the site of the perched channel, which localized lava accumulation in the area and remained consistently active until the TEB breakout [*Patrick et al.*, 2011]. The location of maximum decorrelation duration lies just south of the thickest portion, because the D-vent and rootless shields led to persistent activity in the area long after the July 2007 flow became inactive [*Patrick and Orr*, 2012]. Our data underestimate decorrelation durations for the parts of the flow that entered the vegetation because of the problems with flow identification in this area that are outlined above.

[37] To test the relationship between decorrelation duration and flow thickness, we calculate the average number of days decorrelated within each contour; when this average is compared to the measured thickness of the flow, we find a linear relationship ($r^2 = 0.97$; Figure 12). Here the minimum duration of decorrelation (94 days) reflects the average time

over which the flow was emplaced. Continued decorrelation after flow emplacement is caused by changes in the flow surface after emplacement. Thus the observed relationship between decorrelation duration and flow thickness reflects both post-emplacement processes (such as deflation) and the response of the SAR coherence to these processes. The duration of decorrelation is in part a function of the wavelength used by the satellite, owing to the magnitude of change recognized at increasingly short wavelength. This effect becomes evident when comparing the decorrelation duration of the July 2007 lava flow as viewed using two different SAR satellites. In the ALOS imagery, which uses a wavelength of 23.6 cm, most of the July 2007 flow is correlated after only ~90 days. In contrast, the same flow is decorrelated for ~600 days in the 5.6 cm wavelength Envisat imagery.

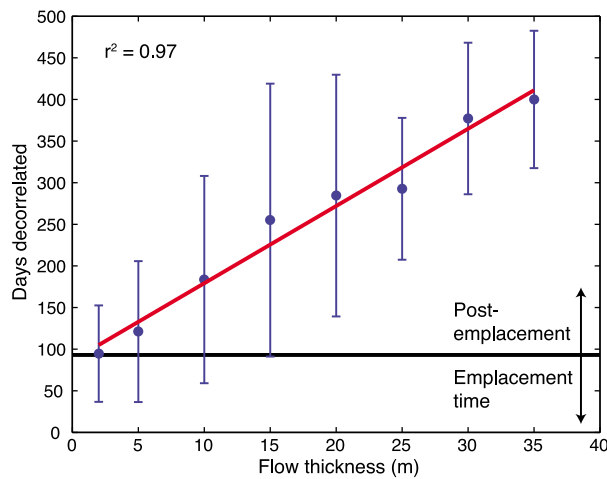[38] The linear relation between flow decorrelation and flow thickness defined by the Envisat images

Figure 12. Comparison of the surveyed flow thicknesses of the July 2007 flow and the average time pixels are decorrelated within each thickness contour from Figure 11. Each point represents the mean length of time a pixel is decorrelated in the areas between each of the thickness contours, while the errors bars show the standard deviation. Error also arises from the uncertain timing of activity due to the duration of the epochs, but it is minor compared to the range in time decorrelated within each contour. The horizontal black line marks the end of emplacement in November 2007. Decorrelation prior to this represents flow emplacement, while continued decorrelation is a product of further change within the flow, including cooling, settling, and subsidence of the flow [*Stevens et al.*, 2001]. Some parts of the flow were emplaced over a period up to 112 days, but the flow edges were correlated after an average of 94 days.

of the July 2007 lava flow can potentially be used to estimate flow thicknesses for any flow in the time series and, when combined with flow areas and flow advance rates, can provide estimates of both flow volumes and average effusion rates. For example, using data for decorrelation durations ≤400 days, we calculate a volume of 62×10^6 m^3 ± 9×10^6 m^3 for the July 2007 flow.

[39] We can compare this to the volume determined from the field survey, calculated by standard GIS methods. First, the GPS data were contoured at 2-m intervals and gridded to derive a digital elevation model (DEM) depicting the upper surface of the new lava field. Then, the DEM of the preexisting topographic surface was subtracted to calculate the residual volume, which corresponds to the bulk-rock volume of the lava flows mapped, about 58×10^6 m^3 emplaced between July 21 and October 16, 2007 (87 days). We estimate the error of this volume to be about 10 percent.

[40] The SAR- and field-based values correspond well, although the comparison is approximate because of underestimates of flow extent in the SAR coherence map (because of vegetation) and continued activity in the flow field until the end of November, which increased the flow thickness beyond the October measurements. However, it points to the possibility of using remote sensing data to obtain accurate measurements of flow thickness (volume) data that are otherwise time-consuming to obtain from ground-based surveys.

[41] A similar relationship between thickness and duration of decorrelation has been observed in lava flows at Etna, Italy [*Stevens et al.*, 2001]. The origin of the decorrelation signal may lie either in cooling-related contraction [*Briole et al.*, 1997; *Stevens et al.*, 2001; *Lu et al.*, 2005] or changes in the roughness of the lava surface (and scattering properties) because of weathering [e.g., *Kahle et al.*, 1995; *Mazzarini et al.*, 2007]. If a lava flow remains decorrelated after emplacement because it is subsiding faster than the fringe rate for the satellite phase [*Stevens et al.*, 2001], it will become correlated when the subsidence rate slows. Once the flow is correlated, a differential interferogram can be used to measure this subsidence rate. We have generated a differential interferogram that shows deformation of the 2007 lava flow over a 35-day period in 2009 (Figure 13). In this image, the thickest part of the flow is subsiding fastest (shown as darker blue). Moreover, nearly two years after the TEB event terminated the July–November 2007 flow, the subsidence was occurring at a rate of 1.4 mm/day. This is calculated from the range change measured at a near-vertical incidence angle of 18.8° and assuming only vertical motion. A correlation between thickness and subsidence rate has also been observed at Okmok and Etna volcanoes [*Stevens et al.*, 2001; *Lu et al.*, 2005]. Together these data show that the combination of coherence maps and interferograms has the potential to document post-emplacement processes in lava flows.

5. Conclusions

[42] We find that SAR Coherence Mapping (SCM) provides a superb means of documenting lava flow activity in Hawai'i. By combining eight years of data from many satellite tracks, it is possible to map volcanic activity on the east rift zone of Kīlauea at high spatial and temporal resolution. This remote sensing technique has some advantages over traditional field mapping, including a large spatial extent, high spatial
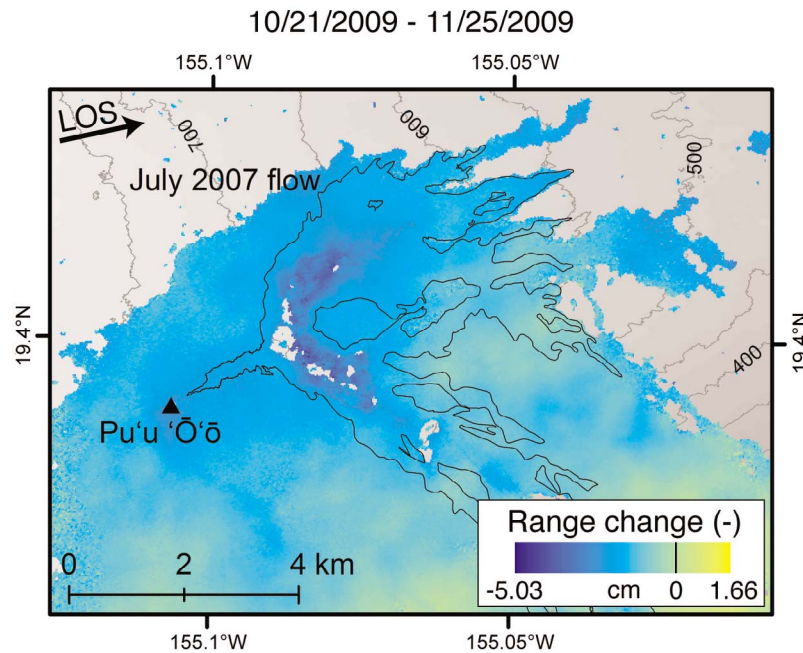
Figure 13. Unwrapped Envisat interferogram from track 322 spanning October 21 to November 25, 2009 shows negative range change from the satellite in centimeters, with blue regions moving away from the satellite. Gray regions contain no data, corresponding to decorrelated areas, while the outline shows the mapped extent on the flow as of November 25, 2009 (T. Orr, personal communication, 2012). The contour interval for the topographic base map is 50 m. The interferogram reveals subsidence of up to 5 cm over the duration of the image assuming all motion is vertical, with 1.4 mm/day at the center of the July 2007 flow two years after emplacement. Some of the range change reflects a topographic component because the DEM was not updated with the morphology of the recent flow. However, this component is likely small (<0.27 cm over the duration of the interferogram) given the small perpendicular baseline of 11.6 m and a maximum increase in elevation of 40 m with the July 2007 flow emplacement [*Massonnet and Feigl*, 1998].

resolution, automation, and the ability to detect activity apart from surface flows. Disadvantages include occasional low temporal resolution, the ambiguity of what decorrelated regions represent, persistent decorrelation masking new activity, and problems with mapping flows that enter vegetation. Overall, this method has the potential to be a valuable tool for monitoring remote volcanoes and to provide a wealth of flow emplacement data for exploring the behavior of lava flows.

[43] Future applications and directions of the SCM method are numerous. This technique can be used to map any form of surface change, such as the extent of ashfalls, floods, landslides, and pyroclastic flows. Furthermore, SAR data from any track of any satellite can be combined to produce the largest possible data set with the highest temporal resolution. We hope that this tool can continue to be developed and facilitate the investigation of many geologic phenomena, as well as lava flow emplacement and volcanic processes.

Acknowledgments

References

Briole, P., D. Massonnet, and C. Delacourt (1997), Post-eruptive deformation associated with the 1986–87 and 1989 lava flows of Etna detected by radar interferometry, *Geophys. Res. Lett.*, *24*, 37–40, doi:10.1029/96GL03705.

Calabro, M. D., D. A. Schmidt, and J. J. Roering (2010), An examination of seasonal deformation at the Portuguese Bend landslide, southern California, using radar interferometry, *J. Geophys. Res.*, *115*, F02020, doi:10.1029/2009JF001314.

Crisci, G. M., S. Di Gregorio, O. Pindaro, and G. Ranieri (1986), Lava flow simulation by a discrete cellular model: First implementation, *Int. J. Model. Simul.*, *6*, 137–140.

Farr, T., and M. Kobrick (2000), Shuttle Radar Topography Mission produces a wealth of data, *Eos Trans. AGU*, *81*, 583–585, doi:10.1029/EO081i048p00583.

Gatelli, F., A. M. Guamieri, F. Parizzi, P. Pasquali, C. Prati, and F. Rocca (1994), The wavenumber shift in SAR interferometry, *IEEE Trans. Geosci. Remote Sens.*, *32*, 855–865, doi:10.1109/36.298013.

Harris, A. J. L., and S. K. Rowland (2001), FLOWGO: A kinematic thermo-rheological model for lava flowing in a channel, *Bull. Volcanol.*, *63*, 20–44, doi:10.1007/s004450000120.

Heliker, C., and T. N. Mattox (2003), The first two decades of the Puʻu ʻŌʻō-Kūpaianaha eruption: Chronology and selected bibliography, in *The Puʻu ʻŌʻō-Kūpaianaha Eruption of Kīlauea Volcano, Hawaiʻi: The First 20 Years*, edited by C. Heliker, D. A. Swanson, and T. J. Takahashi, *U.S. Geol. Surv. Prof. Pap.*, *1676*, 1–28.

Kahle, A. B., M. J. Abrams, E. A. Abbott, P. J. Mouginis-Mark, and V. J. Realmuto (1995), Remote sensing of Mauna Loa, in *Mauna Loa Revealed: Structure, Composition, History, and Hazards*, Geophys. Monogr. Ser., vol. 92, edited by J. M. Rhodes and J. P. Lockwood, pp. 145–170, AGU, Washington, D. C., doi:10.1029/GM092p0145.

Kauahikaua, J. (2007), Lava flow hazard assessment, as of August 2007, for Kīlauea east rift zone eruptions, Hawaiʻi Island, *U.S. Geol. Surv. Open File Rep.*, *2007–1264*, 9 pp.

Kauahikaua, J., S. Margriter, J. Lockwood, and F. Trusdell (1995), Applications of GIS to the estimation of lava flow hazards on Mauna Loa Volcano, Hawaiʻi, in *Mauna Loa Revealed: Structure, Composition, History, and Hazards*, Geophys. Monogr. Ser., vol. 92, edited by J. M. Rhodes and J. P. Lockwood, pp. 315–325, AGU, Washington, D. C., doi:10.1029/GM092p0315.

Kauahikaua, J., K. V. Cashman, T. N. Mattox, C. C. Heliker, K. A. Hon, M. T. Mangan, and C. R. Thornber (1998), Observations on basaltic lava streams in tubes from Kilauea Volcano, island of Hawaii, *J. Geophys. Res.*, *103*, 27,303–27,323, doi:10.1029/97JB03576.

Kauahikaua, J., D. R. Sherrod, K. V. Cashman, C. Heliker, K. Hon, T. N. Mattox, and J. A. Johnson (2003), Hawaiian lava-flow dynamics during the Puʻu ʻŌʻō-Kūpaianaha eruption: A tale of two decades, in *The Puʻu ʻŌʻō-Kūpaianaha Eruption of Kīlauea Volcano, Hawaiʻi: The First 20 Years*, edited by C. Heliker, D. A. Swanson, and T. J. Takahashi, *U.S. Geol. Surv. Prof. Pap.*, *1676*, 63–87.

Lu, Z., and J. T. Freymueller (1998), Synthetic aperture radar interferometry coherence analysis over Katmai volcano group, Alaska, *J. Geophys. Res.*, *103*, 29,887–29,894, doi:10.1029/98JB02410.

Lu, Z., D. Mann, J. T. Freymueller, and D. J. Meyer (2000), Synthetic aperture radar interferometry of Okmok volcano, Alaska: Radar observations, *J. Geophys. Res.*, *105*, 10,791–10,806, doi:10.1029/2000JB900034.

Lu, Z., T. Masterlark, and D. Dzurisin (2005), Interferometric synthetic aperture radar study of Okmok volcano, Alaska, 1992–2003: Magma supply dynamics and postemplacement lava flow deformation, *J. Geophys. Res.*, *110*, B02403, doi:10.1029/2004JB003148.

Massonnet, D., and K. L. Feigl (1998), Radar interferometry and its application to changes in the Earth's surface, *Rev. Geophys.*, *36*, 441–500, doi:10.1029/97RG03139.

Mattox, T. N., C. Heliker, J. Kauahikaua, and K. Hon (1993), Development of the 1990 Kalapana flow field, Kilauea volcano, Hawaii, *Bull. Volcanol.*, *55*, 407–413, doi:10.1007/BF00302000.

Mazzarini, F., M. T. Pareschi, M. Favalli, I. Isola, S. Tarquini, and E. Boschi (2007), Lava flow identification and aging by means of lidar intensity: Mount Etna case, *J. Geophys. Res.*, *112*, B02201, doi:10.1029/2005JB004166.

Orr, T. R. (2011), Lava tube shatter rings and their correlation with lava flux increases at Kīlauea Volcano, Hawaiʻi, *Bull. Volcanol.*, *73*, 335–346, doi:10.1007/s00445-010-0414-3.

Patrick, M. R., and T. R. Orr (2012), Rootless shield and perched lava pond collapses at Kīlauea Volcano, Hawaiʻi, *Bull. Volcanol.*, *74*, 67–78, doi:10.1007/s00445-011-0505-9.

Patrick, M. R., T. Orr, D. Wilson, D. Dow, and R. Freeman (2011), Cyclic spattering, seismic tremor, and surface fluctuation within a perched lava channel, Kīlauea Volcano, *Bull. Volcanol.*, *73*, 639–653, doi:10.1007/s00445-010-0431-2.

Poland, M., A. Miklius, T. Orr, J. Sutton, C. Thornber, and D. Wilson (2008), New episodes of volcanism at Kilauea Volcano, Hawaii, *Eos Trans. AGU*, *89*, 37–38, doi:10.1029/2008EO050001.

Rowland, S. K., A. J. L. Harris, M. J. Wooster, F. Amelung, H. Garbeil, L. Wilson, and P. J. Mouginis-Mark (2003), Volumetric characteristics of lava flows from interferometric radar and multispectral satellite data: The 1995 Fernandina and 1998 Cerro Azul eruptions in the western Galápagos, *Bull. Volcanol.*, *65*, 311–330, doi:10.1007/s00445-002-0262-x.

Stevens, N. F., G. Wadge, C. A. Williams, J. G. Morley, J.-P. Muller, J. B. Murray, and M. Upton (2001), Surface movements of emplaced lava flows measured by synthetic aperture radar interferometry, *J. Geophys. Res.*, *106*, 11,293–11,313, doi:10.1029/2000JB900425.

Wadge, G., P. A. V. Young, and I. J. McKendrick (1994), Mapping lava flow hazards using computer simulation, *J. Geophys. Res.*, *99*, 489–504, doi:10.1029/93JB01561.

Wadge, G., B. Scheuchl, and N. F. Stevens (2002), Spaceborne radar measurements of the eruption of Soufrière Hills Volcano, Montserrat, in *The Eruption of Soufrière Hills Volcano, Monserrat, From 1995 to 1999*, edited by T. H. Druitt and B. P. Kokelaar, *Mem. Geol. Soc. London*, *21*, 583–594, doi:10.1144/GSL.MEM.2002.021.01.27.

Zebker, H. A., and J. Villasenor (1992), Decorrelation in interferometric radar echoes, *IEEE Trans. Geosci. Remote Sens.*, *30*, 950–959, doi:10.1109/36.175330.

Zebker, H. A., P. Rosen, S. Hensley, and P. J. Mouginis-Mark (1996), Analysis of active lava flows on Kilauea volcano, Hawaii, using SIR-C radar correlation measurements, *Geology*, *24*, 495–498, doi:10.1130/0091-7613(1996)024<0495:AOALFO>2.3.CO;2.

Zebker, H. A., P. A. Rosen, and S. Hensley (1997), Atmospheric effects in interferometric synthetic aperture radar surface deformation and topographic maps, *J. Geophys. Res.*, *102*, 7547–7563, doi:10.1029/96JB03804.